Alessio Bucciarelli, Silvia Chiera, Alberto Quaranta, Vamsi K. Yadavalli, Antonella Motta, Devid Maniglio
A Thermal-Reflow-Based Low-Temperature, High-Pressure Sintering of Lyophilized Silk Fibroin for the Fast Fabrication of Biosubstrates, Advanced Functional Materials, 29 (42), 1901134, 2019
10.1002/adfm.201901134

A thermal-reflow based low-temperature, high-pressure sintering of lyophilized silk fibroin for the fast fabrication of bio-substrates.

A. Bucciarelli[*], *S. Chiera, A. Quaranta, V.K. Yadavalli, A. Motta, D. Maniglio*[*]

A. Bucciarelli, S. Chiera, Prof. A. Motta, Dr. D. Maniglio

Department of Industrial Engineering, University of Trento, via Sommarive 9, Trento, Italy.

BIOtech Research Center, Italy and European Institute of Excellence on Tissue Engineering and Regenerative Medicine, Via Delle Regole 101, Trento, Italy.

E mail: Alessio.Bucciarelli@unitn.it, Devid.Maniglio@unitn.it

Prof. A. Quaranta

Department of Industrial Engineering, University of Trento, via Sommarive 9, Trento, Italy.

Dr. V.K. Yadavalli

Department of Chemical and Life Science Virginia Commonwealth University 601 West Main St., Richmond, VA 23284-3028, USA

Abstract

Solid-fibroin is a bulk non-porous material that can be prepared with two methods: a liquid- gel-solid transition from a fibroin solution or a sintering procedure starting from silk powder. Both methods have their own disadvantages: the first requires several weeks and the process is size dependent, the second require high temperatures. In this work, to overcome these limitations we propose a low temperature sintering procedure based on a thermal-reflow to produce in fast fashion monoliths of solid-fibroin. Thermal-reflow is a well-known mechanism that takes place when the glass transition temperature of the material is lower than the temperature used to process it. Water plays an important role decreasing the glass transition temperature down to 40 °C. For the first time, a thermal reflow was conducted on lyophilized silk fibroin at 40 °C, associating to the water addition a high-pressure compression. To optimize the process a full factorial design of experiment was used. The material was then studied in the crucial phases by DSC, FTIR and SEM, proving that the thermal-reflow can occurs on fibroin with low crystallinity even at a low temperature if driven by a high-pressure process. Finally, a mechanical characterization, and a preliminary in vitro test were conducted.

1. Introduction

Over the last two decades, the protein fibroin from the silkworm has been used to produce a variety of materials with a wide range of advanced applications. Due to the unique combination of properties such as mechanical strength and toughness[1–3], biocompatibility[4–6], biodegradability[4–7], thermal stability[8], and easy processability[5,9], regenerated silk fibroin has been used as a functional biomaterial, when a positive interaction with living tissue is required. This has ranged from tissue engineering and regenerative medicine[4,10,11] to biosensing[12–17]. While a plethora of micro and nanoscale architectures of silk fibroin have been explored in literature - films, fibers, microparticles and gels[18], building larger, macroscale objects of fibroin has been challenging. Only recently a method to produce bulk-fibroin monoliths based on solvent evaporation of fibroin solution (*solid-fibroin by casting*) has been proposed[19]. During room temperature evaporation fibroin protein suspension undergoes a sol-gel-solid transition[20,21], triggered by nucleation and aggregation phenomena that are generally slow: from several weeks using a water solution to several days using a hexafluoroisopropanol solution. The mild conditions in which this material can be produced and the facile embedding of biomolecules, as enzymes, make *solid-fibroin by casting* suitable for the fabrication of surgical implants.[22] However, the time necessary to completely evaporate the solvent and the large shrinkage of the monoliths constitute a limiting factor for large size objects and large scale production. These limitations could be overcome by adopting a sintering method, already proposed in few works in literature, but effectively not fully understood[23–25]. In those works, the authors propose the compression of fibroin powder in molds at high temperatures to obtain a solid material in few minutes[23,24]. While in the conventional sintering approach, the temperature to achieve the full compaction of dry fibroin powder has been reported to be 200 °C[23], introducing a pulsatile electric potential (pulse-energizing sintering) and wet powder the temperature could be decreased down to 100 °C[24]. A more recent work proposed the compression of wet silk powder, produced by milling, in a temperature range of 150-180 °C[25]. However this temperature remains too

high to allow the incorporation of thermally degradable molecules, such as drugs or enzymes[26], and the introduction of electric field represent an unnecessary process complication. In literature, the transition mechanism occurring during sintering is not yet fully explained, however it was supposed that both glass transition temperature (T_g) and the secondary structure could play an important role[24,25]. In particular, other works report that thermal-reflow (thus a significant molecular interdiffusion) can occur only at temperatures higher than T_g[27–29]. Water, in this phenomenon, acts as plasticizer decreasing the glass transition temperature (T_g)[27–29] and, consequently, the energy needed to activate thermal-reflow[30]. On wet fibroin films, this principle has been used to imprint microstructures[31] and hydrolysable metal microstructure using a hot mold[32], to produce laminates of staked films by compression[33], and, more recently, to produce a fibroin device with programmable degradation time[34]. Even if the T_g of fibroin is reported to decrease down to 40 °C in some conditions, none of the above processes report the use of a such low temperature. Instead, to activate thermal-reflow, silk fibroin films are usually treated at 120-140 °C. In addition, to date, no study reports the possibility of a thermal-reflow on lyophilized fibroin. Temperature, pressure (application of stress) and water content can also influence the secondary structures inducing the transition to higher stability crystalline phase[29,35,36]. In the case of sintering process the use of intrinsically crystalline fibroin powder led to the necessity to increase temperature up to 200 °C to obtain satisfactory thermal reflow [24,37,38]. In this work we propose a low-temperature sintering (LTS) procedure, in which the compaction of a lyophilized fibroin is achieved at 40 °C in few minutes, leading to solid monoliths (low temperature sintered fibroin, LTS fibroin). The process is based on the use of lyophilized silk fibroin with a low crystallinity together with the fast addition of water by moisture adsorption. The fast addition of water permits the decrease of T_g, plasticizing the powder without inducing crystallization before compression. This allowed us to report, for the first time, the possibility to activate thermal-reflow on lyophilized silk fibroin at the process temperature of 40 °C.

2. Results and Discussion

The study of the production of a solid material from regenerated silk fibroin using a fast and cold compression is important to provide a suitable method for the development of a new generation of biomaterials. Understanding how the process parameters influence the final material and in which direction the solid-solid transition occur gives useful insight on the process and allow to determine the optimal procedure to form full sintered object. To this purpose, a screening was done using a 2^4 full factorial design of experiment (DOE). Each variable is unambiguously associated to a factor as reported in **table 1**: from here on the term factor will be used interchangeably with variables. To follow the process optical and a mechanical measurement has been selected: the first allows to follow the fibroin transition from white reflective to a transparent material, the second from soft to hard. The overall results of the analysis are listed in **table 3S**, where the 16 samples are listed with their associated yields. The structural and thermal analysis on the fibroin collected form the main stages of the optimized procedure allowed us to reveal useful insight on the molecular transition occurring during the process. In particular, to underline the importance relative amounts of the different secondary structures in the successful application of our method. FTIR has been conducted on samples with different duration of the moisture absorption phase: we demonstrated that an excessive duration induces a stabilization due to a transition into the more stable β structures thus avoiding the solid-solid transition during the compression. The DSC analysis reveals that the glass transition temperature does not change after the water addition on the lyophilized material but decreased after the compression. These allows us to hypotize a decreasing of T_g under the process temperature and consequently the possibility of a thermal-reflow. This hypothesis was further confirmed by the SEM microstructural analysis during different time points in the compression. Preliminary in vitro test was performed in order to evaluate cell adhesion. All samples promoted a fast adhesion, but at day 5 cells cultured on LTS surfaces showed a more osteoblastic-like morphology and cytoskeleton organization.

2.1 Process optimization: Optical Method

An optimal transformation of the silk fiber powder into a solid compact material by compression molding implies the turning of a shiny white solid (reflecting and scattering light) into a compact yellowish, partially transparent material. This change in the optical behavior of the material can be used to evaluate the quantity of sintered material. In particular, the area of the absorbance spectra in the visible region (400-700 nm) is related to the presence of inhomogeneities in the structure. So, the lower the area of the absorbance spectrum, the higher the amount of fibroin undergone to transition. Based on the results obtained from the UV-VIS spectra (see **figure 1S**) an empirical predictive model was built. This model (see **table 2S**) reports the value of the area under the spectra (in the visible range) as function of the considered variables (**figure 2**). Based on this model the analysis of variance (ANOVA) was done to evaluate its significance and the significance of terms included. The ANOVA test (see **table 2S**) shows that the built model is significant so, it can be used to predict the trend of the yield. The results of our predictive model are shown in **figure 3** as contour plot. The lower area is obtained for a 120 s ramp time a pressure of 400 MPa, with a maintenance time of 1200 s, and in presence of 20% of water. The addition of water ensures better results with a VIS area in the range of 150-400, instead, in absence of water the range increases to 400-560. This can be also noted by a simple comparison between the samples presented in **figure 2** of the supplementary material: the quantity of lyophilized white fibroin dramatically decreases passing from the right to the left column. It's worth noting that in presence of water the absorbance spectrum area decreases with the decreasing of the ramp time. We can explain this phenomenon considering that, since the transition to solid is promoted by the presence of water, a high compression rate forces the water to diffuse into the spongy lyophilized fibroin, prior to the transition to the solid phase, allowing a more homogenous compaction of the structure. Instead, a low compression rate induces the transition at the surfaces first (where the percentage of adsorbed water is higher) preventing the transition of the core. In absence of adsorbed water, instead, the absorbance area decreases with the increasing of the ramp time: the transition

occurs in all the material and probably it starts where the local presence of water is higher, giving, as a result, a material in which solid and lyophilized phases are mixed together in a continuous fashion. In this case, a higher amount of time allows the transition of a higher amount of material. The effects of the maximum applied pression is, instead, independent to the water presence but related to the ramp time: the absorbance area decreases with the increasing of the maximum applied pressure, but the amount of this decreasing depends on the ramp time. Both the higher order mixed terms t_{ramp}*P_{max} and t_{ramp}*t_{maint}*$m_{w\%}$ (**table 2S**) determine the presence of the curvature. The ramp time and the maximum applied pressure are correlated by the presence of the term t_{ramp}*P_{max}: upon this finding we can hypothesizes that the important term is the compression rate (A/B), confirming that the process, as could be expected, is sensitive to the kinetics. Is worth noticing when the maintenance time is 0 a threshold pressure is present: above it the area increase in the same direction of the increasing of the ramp time; instead, below it the direction is inverted. This pressure can be estimated in 377 MPa in case of 20 % of added water, and in 330 MPa in case of no water addition.

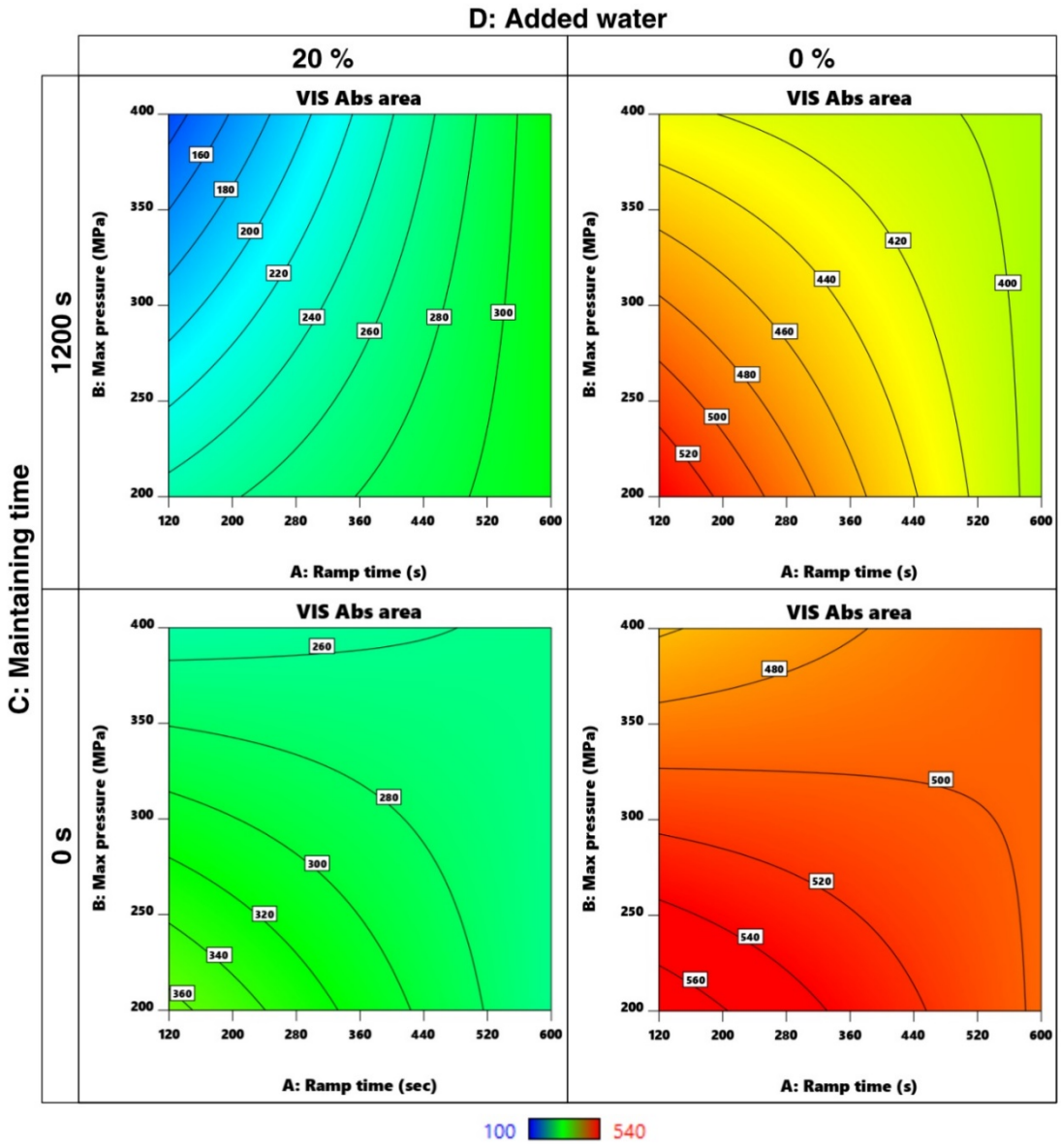

Figure 1: Contour plots based on the empirical model that report the trend of the area under the visible part of the absorbance spectrum (400-780 nm) versus the considered variables. This allows to establish the optimal process conditions. In this case the lower area can be obtained with a low ramp time (t_{ramp}=120 s), a high pressure (P_{max}=400 MPa), a high maintenance time (t_{maint}=1200 s), and with the presence of added water ($m_{w\%}$= 20 %).

2.2 Process optimization: mechanical method

The mechanical properties of the sample changed during the process: from the a spongy soft to a hard-solid material. Due to this difference, a mechanical compressive test can also be used as an evaluation of the amount of sintered material. The results of the compressive test on the 16 samples is reported in **figure 4S** as stress-strain curves. The value of the Young modulus was obtained from the linear part of the curves and used as yield to find a correlation with the process parameters. An ANOVA test (**table 3S**) was preformed, revealing that the model is significant. The contour plots of **figure 3** shows the results of the predictive model. The higher Young modulus is obtained, for t_{ramp}=120 s, P_{max}=400 MPa, t_{maint}=0 s, and $m_{w\%}$=20 % of water. It worth to notice that the result predicted changing the maintaining time to 1200 s is not so different from the previous conditions, indicating the fact that the maintaining time is not significant (**table 3S**). As a general trend the Young modulus increase with the increasing of the maximum applied pressure. In case of water addition this increment is in direction of the decrease of the ramp time; instead, in case of absence of added water the direction is the opposite: Young modulus increases proportionally with the ramp time. This complex behavior is due to the presence of the mixed term t_{ramp}*$m_{W\%}$ (**table 3S**) and it could be explained considering that water changes the overall kinetics of the process. In presence of added water, a high compression rate allows its diffusion into the sample and a full transition of the lyophilized fibroin into the solid state. The term P_{max}*t_{maint} (B*C, **table 3S**) is probably due to the fact that a high pressure for a prolongated time, even if allows a complete transition, decreases its compressive modulus and, probably, damages the sample. In absence of added water, a longer ramp time is necessary to obtain a better compaction and a higher mechanical strength. In conclusion, considering the fact that the maintaining time is not so influent on the Young modulus, to minimize the optical yield while maximizing the mechanical one, optimal parameters should be set as follows: t_{ramp} = 600 s, P_{max} = 400 MPa, t_{maint} = 1200 s, and $m_{w\%}$ = 20 %.

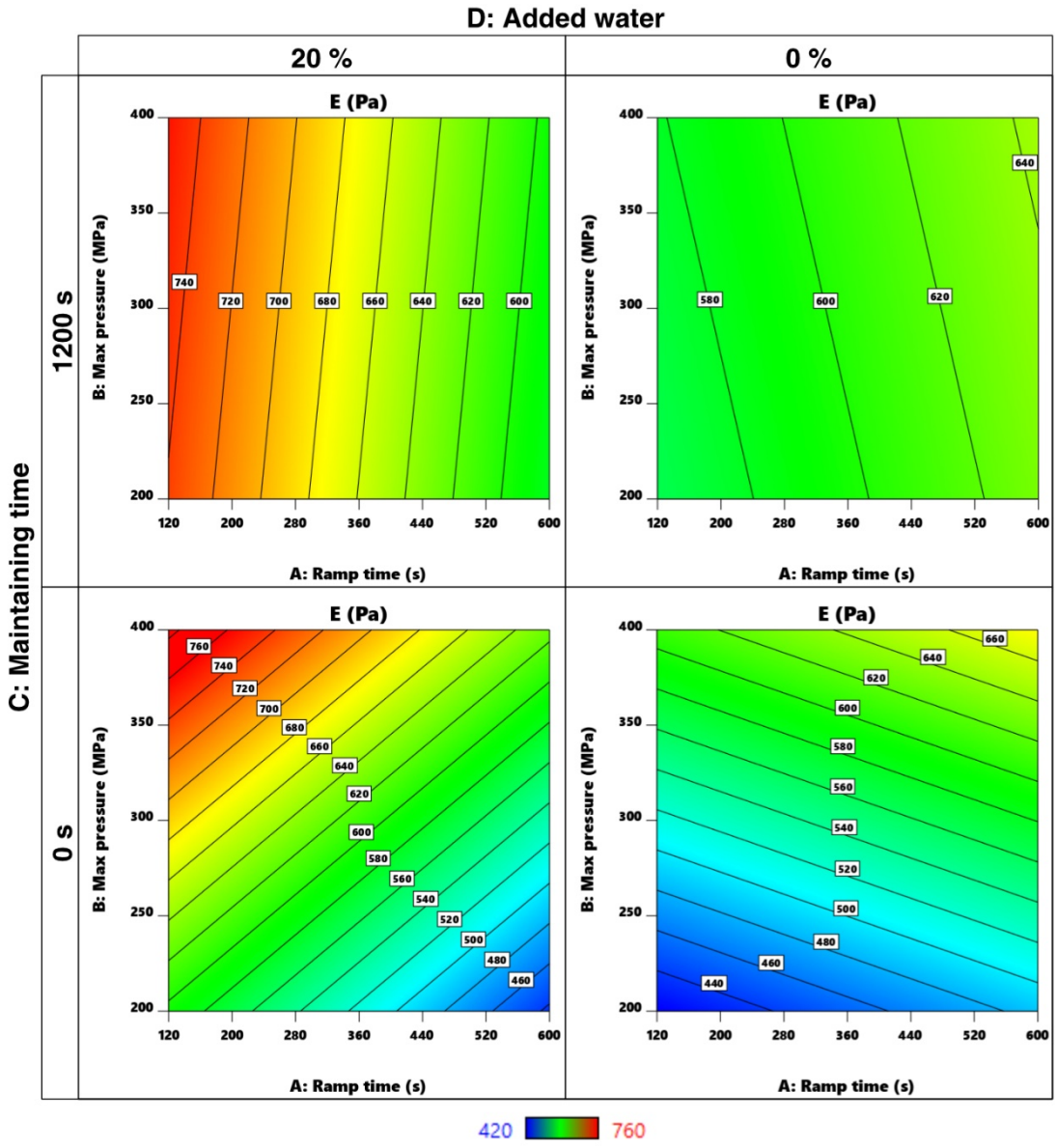

Figure 2: Contour plots based on the empirical model of the compression Young modulus as a function of the considered variables. This allows to predict in which direction the transition from lyophilized to solid silk fibroin occurs. In this case the maximization of the Young modulus can be obtained with a low ramp time, a high pressure, a low maintenance time, and with the presence of added water. However, since the maintaining time is not so significant on the Young modulus, in order to contemporary minimize the optical yield, the final choose parameters for the optimized process are: t_{ramp} *= 600 s,* P_{max} *= 400 MPa,* t_{maint} *= 1200 s, and* $m_{w\%}$ *= 20 %.*

2.3 Compression test

Bones and all the object used in osteo-fixation are usually subjected to mechanical stresses then, to evaluate the response of our material, we performed a preliminary compression test. The compression modulus was evaluated on 3 samples produced by the optimized procedure in two conditions: after drying the samples in a desiccant chamber at 25 °C for 2 days (dried), and immediately after a 6 h immersion in water at 37 °C, to simulate physiological conditions (physio). In accordance with a previous study, our results plotted in **figure 4 (A)**, shown a dramatically decrease of the compression modulus in simulated physiological conditions: the modulus passed from 1120 ± 130 MPa (dried) to 205 ± 130 MPa (physio). This effect can be attributed to plasticizing effect of water. As result the samples, as can be seen in **figure 4 (B)**, during the compression test were strongly deformed, passing from 8 mm to 1.2-1.5 mm of diameter, without braking.

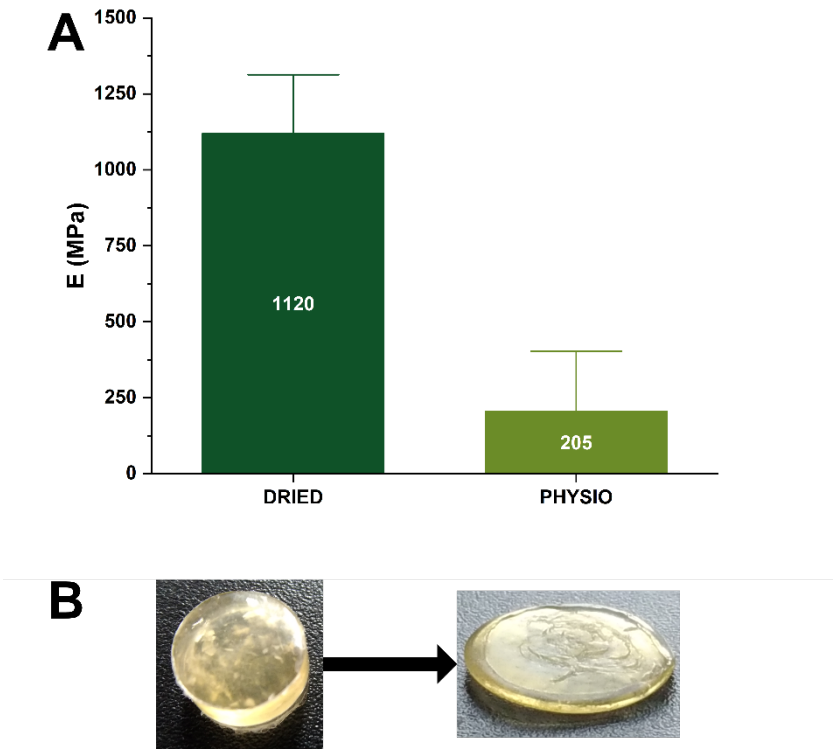

*Figure 3: (**A**) Compression modulus in normal condition (20% of humidity, 25 °C) and physiological condition (after 6h in water at 37 °C). The test was performed on 3 samples per each condition. As can be seen due a drastic reduction of the modulus is present in the simulated physiological conditions: this could be attributed to the plasticizing effect of the water. (**B**) Sample before (on the*

right) and after (on the left) compression, as can be seen the sample is deformed during the test, no brakes occur.

2.4 Structural analysis

On the optimized process the secondary structure was evaluated by FTIR in the three main stages: after lyophilization, after the exposure to moisture, and after compaction. The comparison between the different spectra, in the range of the primary and secondary amide peaks, is shown in **figure 5 (A)**. After the water treatment we should distinguish between the external part of the fibroin cylinder and the internal part. The rapid addition of water via moisture absorption does not significantly affect the secondary structure inside the cylinder of lyophilized fibroin, since the water cannot reach the inner center within a so low amount of time: in this case the spectra (**figure 5 (A),** Water treat in) remains unchanged with respect to those collected after lyophilization (**figure 5 (A),** Lyo). On the other hand, on the surface (**figure 5 (A)**, Water treat out) the FTIR spectra show an increment in the intensity at 1620 cm^{-1} for the primary amide, and at 1538 cm^{-1} for the secondary amide: both are related to an increment of the amount of β-sheet structure[39]. After the compression (**figure 5 (A)**, LTS) the intensities of the spectra at 1620 cm^{-1} and at 1538 cm^{-1} decreases as an effect of the interdiffusion of the surface and the inner part of the lyophilized silk fibroin cylinder. So, no more differences can be detected between the surface and the core. No significant changes have been found in the intensities at 1700 (β-sheet), 1648 (random), and 1620 cm^{-1} (random). So, in order to quantitively evaluate the changes in the secondary structure, a more accurate analysis was conducted on the deconvoluted primary amide peak. **Table 2** shown the peaks position and the assigned secondary structure, **figure 5 (B)** show the deconvolved curves and **figure 5 (C)** the perceptual amount of each structure in the different phases of the process. These analyses reveal that the water treatment conducted for 30 m (**figure 5 (C)**, 30m) increases the amount of native β-sheet (peak centered around 1630 cm^{-1}) on the cylinder surface (35 %) and in a smaller amount also in the inner part (26 %), this is accomplished by a decrement of the random coil and β-turns. Instead parallel and

antiparallel β-sheet does not significantly change during this stage. After the compression the secondary structure results to be homogeneous. In fact, a "mean" composition between the two analyzed (external and internal) after the water treatment should be expected. This is true for the random coil structure, resulting 26 % in amount, the exact mean between the 31 % of the surface and the 20 % of the internal part. On the contrary, the native β-sheets amount decreases of about 19 % compared to the mean (29.7 %) and both the parallel and the antiparallel β-sheets increase of an amount of 7.3% and 1.3 % respectively (compared to the mean values 7.4% and 9.4 %). In addition, the alpha helices are formed in an amount of 6 %. We can hypothesize that the stabilization due to the β structure before the compression plays an important role in the possibility for fibroin to undergo to solid-solid transition. To prove this hypothesis, we left a sample of lyophilized silk fibroin in the humidostatic chamber overnight, then we tried to produce a sintered sample without success. The reason can be due the transition occurred between β-native and β-parallel structures. As can be noticed from **figure 5 (C)**, passing from a 30 m to 12 h of moisture exposition there was a significative increase in β-parallel (from 8.8 to 35.9 %) and decrease in β-native (from 34.9 to 10.9 %) structures: this transition could explain the stabilization of silk fibroin due to water exposition, differentiating the natural material from the treated one. As a negative result, when we compressed the sample exposed 12 h to moist, the molecular interdiffusion did not occur, even if applying the best process conditions. To explain this effect we observed that the deconvolution of the primary amide peak of the material post-compression (**figure 5 (C)**, LTS 12h) had only few differences in the secondary structures if compared with the it with the pre-compression (**figure 5 (C)**, 12h): an increasing in the amount of β-turn (from 20.6 to 25.5 %) and β-antiparallel (from 8.6 to 12.6 %) and a slightly decrease in the amount of random coil (from 23.3 to 21.1 %) and β-parallel (from 35.9 to 31.4 %). We can attribute the impossibility of a thermal-reflow to the large amount of β-parallel structures that, due to their high conformation stability, can withstand the external applied force without undergo conformational change.

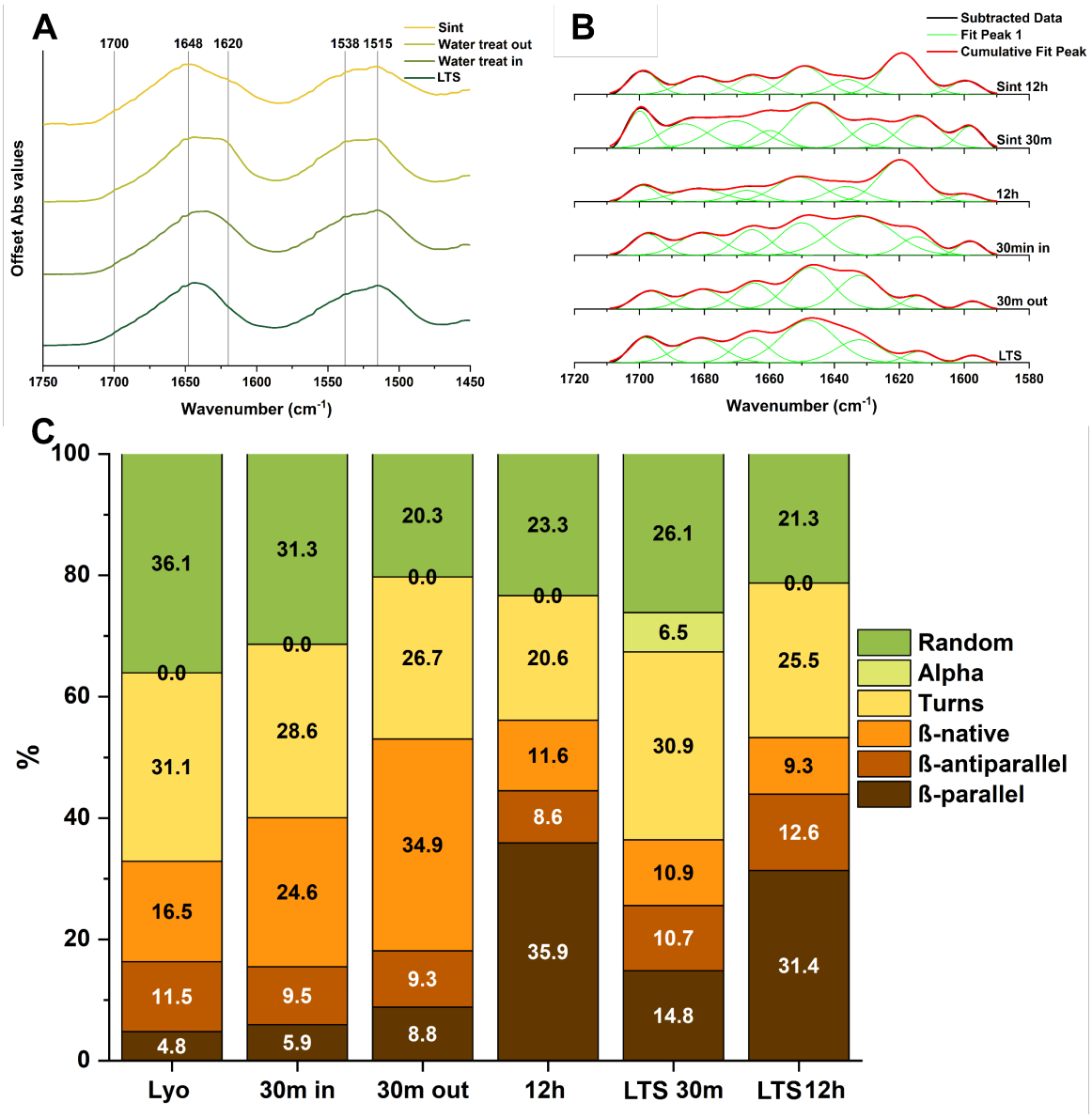

*Figure 4: (**A**) FTIR ATR spectra of the fibroin collected after the three principal stages of the process: the lyophilization (Lyo), the water treatment both on the surface (Water treat out) and the inner part (Water treat in) of the silk fibroin cylinder, and after compression (LTS). The wavenumber associated with the β-sheet structure are 1700, 1620, and 1538 cm^{-1}, instead 1648 and 1515 cm^{-1} are associated with the random structure. The water addition increases the amount of β-sheet especially on the surface. After the compression a "mean" secondary structure between the two obtained after the water addition is found: the compression phase allows the interdiffusion of the material, generating a uniform solid. (**B**) Deconvolution of the amide primary peak and (**C**) percentage of the respective area (on the bottom). The analyzed samples are: dry lyophilized silk fibroin (**Lyo**), internal part after 30 m of moisture exposure (**30m in**), external part after 30 m of moisture exposure (**30m out**), after 12 h of moisture exposure (**12h**), 30m exposed sample after compression (**LTS 30m**), 12 h exposed sample after compression (**LTS 12h**). The water treatment on lyophilized fibroin results in an increment of the native β-sheets and as a consequence in a decreasing of the random structure. The inner part of the lyophilized cylinder results less susceptible to the water addition. After compression the alpha helix structure is formed and the amount of parallel and antiparallel β structure increases, while the amount native β-sheet structure decreases.*

2.5 Thermal analysis

Differential scanning calorimetry in the range of 40-320 °C, shown in **figure 6 (A)**, has been used to evaluate the glass transition temperature (T_g)**.** Lyophilized silk fibroin (Lyo) shows a T_g around 180 °C (black arrow), followed by an exothermic peak of crystallization with the maximum centered around 225 °C (red arrow, ΔH = 3.45 mJ/mg). The loss of water and the degradation peaks maximum are at 100 °C (ΔH = 20.63 mJ/mg) and at 285 °C (ΔH = 27.34 mJ/mg). A T_g at 65 °C (black arrow) can be identified after compression (LTS). In this case nor the water peak, neither the crystallization peaks are present, indicating the absence of both water in the network and structural transitions to the crystalline form. The degradation peak is in the same position as the lyophilized sample, with a maximum at 285 °C (ΔH = 29.16 mJ/mg). The T_g cannot be detected for the material exposed to moisture: the presence of water and the thermal treatment of the DCS process, in fact, can plasticize the material, and because only a little amount of random structure remains is extremely difficult to determine the glass transition temperature. In this case, the water peak has a maximum at 85 °C (ΔH = 25.38 mJ/mg) with a larger area as a consequence of water addition, while the position of degradation peak remains, also in this case, unchanged, with a maximum at 285 °C (ΔH = 19.24 mJ/mg). To correctly estimate the position of T_g, a modulated DSC was performed on this material. The reversible, non-reversible, and total heat flows are shown in **figure 6 (B)**. The T_g can be detected in both the total and the reversible heat flow signal around 180 °C (black arrows). We can conclude that the rapid exposure to water moisture doesn't change the glass transition temperature of the lyophilized fibroin and the decrease of the T_g on the solid protein is obtained during the compression phase; this is accordance with the previous result obtained by the optical and the mechanical DOE in which the significance of mixed term involved the water addition has been uncovered (for the optical method A*C*D , A*D, for the mechanical method A*D C*D ramp time*max pressure).

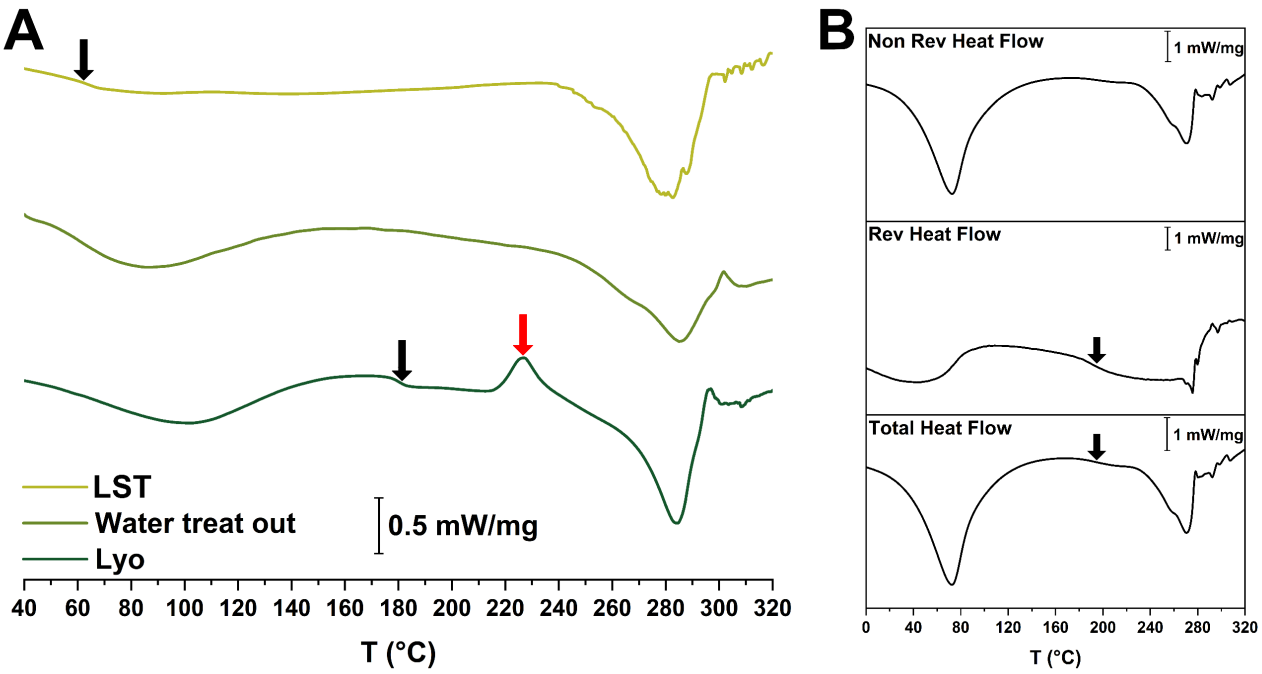

*Figure 5: (**A**) Digital scanning calorimetry of the sample after the three main stages of the process: the lyophilization (Lyo), the water addition (Water treat out) and, the compression (LTS). The black arrows indicate the position of the glass transition temperature (T_g): for the lyophilized silk fibroin that temperature is at 180 °C, for the sintered sample at 65 °C, no glass transition is recorded for sample after water treatment. A clear crystallization peak is present in the heat flow of the lyophilized silk fibroin at 225 °C (red arrow). The absence of these peaks on both the other curves indicate that the amorphous structures has transited to the crystalline one. (**B**) Modulated DCS of the water treated sample. The reversible and the total heat flow show a T_g around 180 °C, the same position of the one reported for the lyophilized sample. The rapid exposition of lyophilized silk fibroin to water does not change the glass transition temperature.*

2.6 Microstructural analysis

We observed the thermal-reflow at the microstructural level by following the compression test at different time points (0, 40, 80, and 120 s). The SEM micrographs shown in **figure 7** reveals the formation of planes perpendicular to the compression direction (indicated with the black arrows). Separated planes are visible at low magnification (column 1) in the pre-compressed sample (0 s) and after just 40 s they appear to be collapsed. After 80 s the planes are no longer visible; instead some ripples along the compression direction (80 s, 100 X) indicate that the planes are melted together, and the overall structure is more compact. After 120 s the structure is fully compact: no more plane or ripples are recognizable, and the microstructure shows the typical appearance of a brittle fracture (120 s, column 1). At higher magnification (column 2) we could observe the thermal-reflow taking place: nanometric ripples appear after the pre-compression (0 s), with a crest to crest distance in 288 ± 15 nm; at 40 s we could observe ripples structure in the micrometric scale, in this case the estimated crest to crest distance is 3 ± 1 μm; this kind of structure is no more visible at 80 s where, we can observe only few crest in a compact material; at 120 s the material is fully compacted. The overall process can be a flow of material that, from the micrographs, seems to be a sort of viscous fluid until it reaches a solid form, this is compatible to previous studies that reports this phenomenon when fibroin temperature is raised above the T_g.

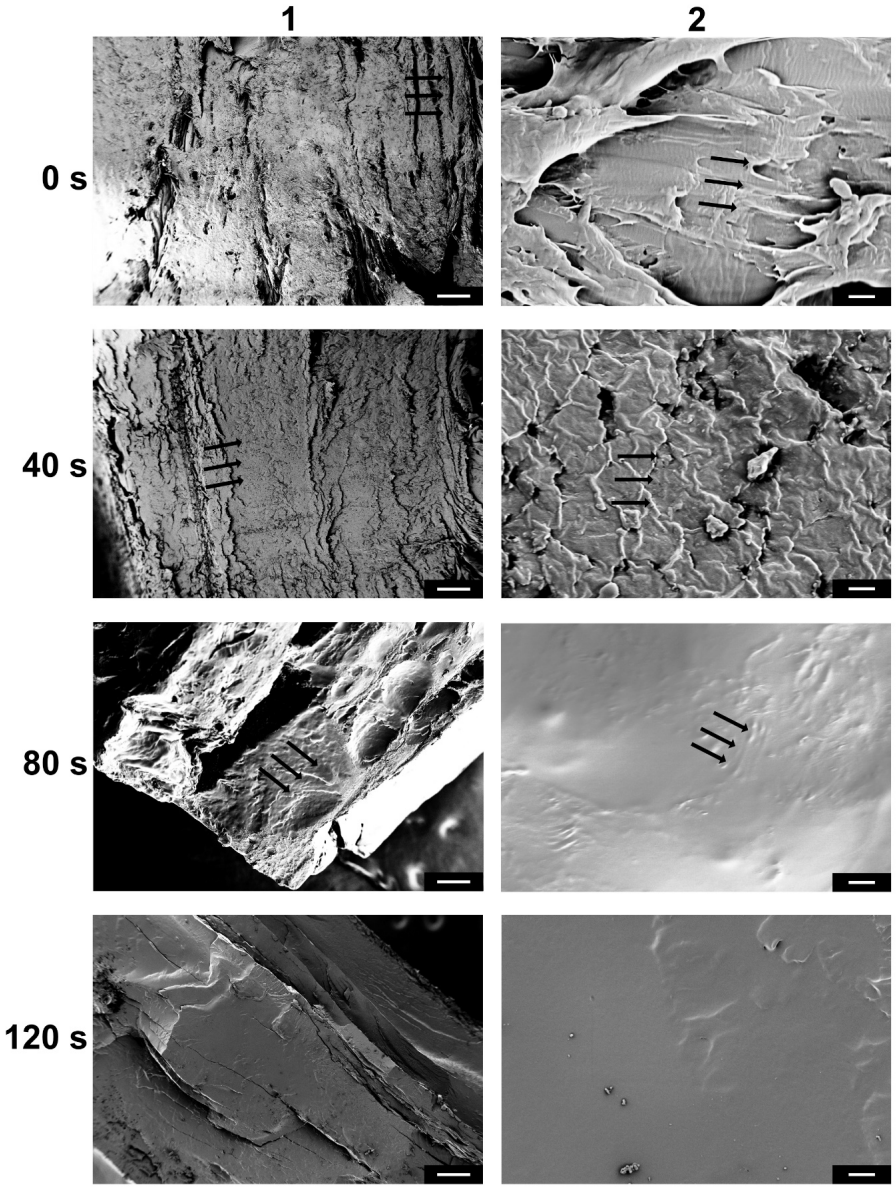

Figure 6: SEM micrographs during different time points on the optimized compression phase: just after the pre-compression (0 s), then at 40 s and 80 s, and at the end of the process (120 s). The black arrows indicate the direction of the compression (detectable from the stratified structure formed during the process). In particular, the "planes" are perpendicular to the compression. These structures can be clearly recognized in the pre-compressed material (0 s) and in the first time point (40 s), in the lower magnification (column 1). At higher magnification (column 2) we can observe the viscous flow occurring, the formation of ripples (40 s) and their flow (80 s), forming a compact material (120 s). The flow is visible also at higher magnification (80 s, column 1), where the material seems to be in sort of melted state. After 120 s the material results to be compact (120 s column 2), with typical microstructure of a brittle fracture (120s, column 1). Scale bar are 250 µm for column 1, and 2 µm for column 2.

2.7 *In vitro* cell culture and confocal imaging

As depicted from **figure 8**, cells were in general able to homogenously adhere and populate all sample surfaces starting from day 1. However, at day 5 LTS and PCL surfaces influenced cell adhesion in terms of spreading degree and cell density. Cell adhered to PCL with high density but with a low degree of spreading, assuming a more spindle shape fibroblastic-like. On the contrary, a lower cell density to LTS fibroin samples was seen, inducing a higher spread, cytoskeleton distribution and adhesion shape osteoblastic-like. It should be noticed that, according to the increasing number of cells, there are visible fiber structures mainly from day 3 on both type of samples, colored in green (CytoPainter Phalloidin-iFlour 488 dye), that are corresponding to the stress fibers typically characterizing cell cytoskeleton. They are mainly composed by actin and they usually play an important role in particular in cell adhesion. Cells nuclei, colored in blue (DAPI dye), are difficult to detect in the LST samples. In fact, DAPI and silk fibroin are both exited in the same range of wavelength and they also emit in the same spectral region. As result of the fibroin autofluorescence the material underlying the cells is visible and of the same color of the cell nuclei. However, cell cytoskeleton, colored in green (CytoPainter Phalloidin-iFlour 488 dye), is evident in both LST and PCL samples.

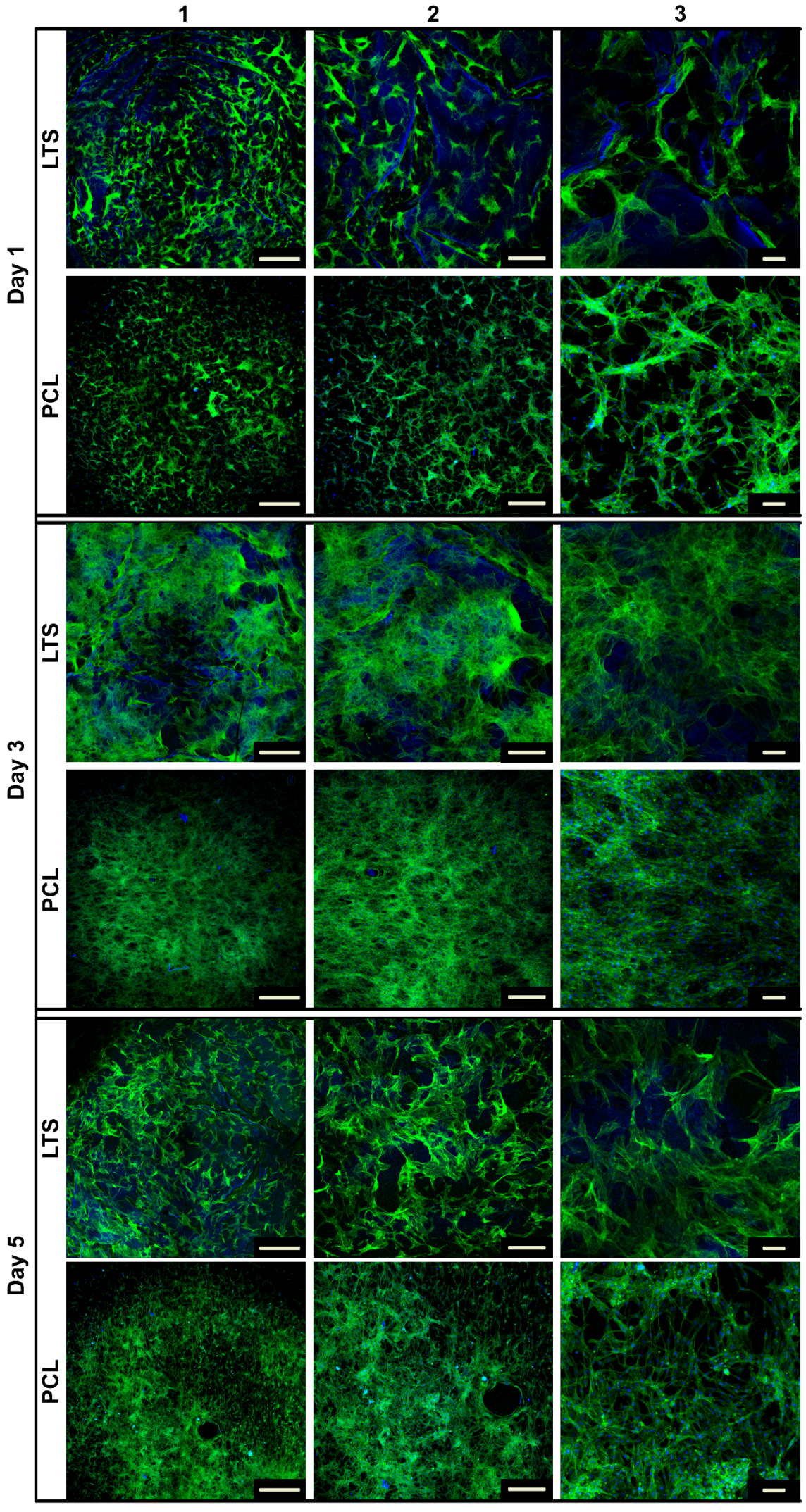
1
2
3
Day 1
LTS
PCL
Day 3
LTS
PCL
Day 5
LTS
PCL

Figure 7: Confocal microscopy images of adhered cells at different time points on both types of samples at three different magnifications. AdMSCs cytoskeletal morphology and distribution (green staining cytoskeleton, blue staining DAPI and LTS fibroin samples). Scale bar are 1000 µm for column 1, 500 µm for column 2, and 100 µm for column 3.

2.8 Discussion

As evidenced by the described results, the sintering process of fibroin at low temperature is influenced by several parameters: the treatment temperature, the maximum applied pressure, the ramp time to the maximum pressure, the pressure maintenance time in and the amount of adsorbed water l. In order to understand which of them are more important to complete the transition from lyophilized to solid fibroin, a screening process was essential. The screening was performed using a design of experiment (DOE), a method that allows to build a model for a process capable of correlate the variables and their combined effect, to one or more yields specifically chosen to describe it. The optimal process conditions were found at the higher pressure (400 MPa), maintaining time (1200 s) and percentage of added water (20%), and the lower ramp time (120 s). In order to understand why this solid-solid transition occur at molecular level we performed a structural and thermal analysis on the material in three stages of the optimized process: after lyophilization, after the addition of water using moisture, and after the compression stage. These analyses revealed that the rapid absorption of water by lyophilized fibroin doesn't change the glass transition temperature. So, it is possible to obtain a thermal-reflow even if the temperature is lower than T_g. The three main stages were studied to understand the reason why the solid-solid transition occurs from the structural, thermal and microstructural point of view. In the first step, fibroin water solution, prepared by the conventional protocol, is rapidly frozen to preserve its denaturated status and then lyophilized to remove water (**figure 1 (A)**, step 2). The obtained lyophilized fibroin structure is mostly in a random coil, β-turn, and β-native configurations, only in minor part composed by β-parallel and antiparallel structures (**figure 5 (C)**, Lyo). In the second step, a single block of the solid is exposed to water moisture for 30 min inside a chamber with controlled temperature and humidity (**figure 1 (A)**, step 3). Water,

adsorbed from the surfaces, results to decrease in content moving in the inner part, therefore the content of the overall β-structures (native, parallel and antiparallel), formed for the stabilizing effect of water vapor, follows the same gradient (**figure 5 (C)**, 30 min in and 30 min out). Is worth to notice that this treatment increases significantly the β-native structures, and, in minor extent, the β-parallel, while β-antiparallel are slightly decreased. No significant variation of the glass transition temperature could be found, even if the DSC has been performed on a sample taken from the surface thus with a higher content of water (**figure 6 (B)**, reversable heat flow). Interestingly, this result seems to be in contrast with previous literature results in which, due to the water absorption the T_g of fibroin films was decreased down to 40 °C. However, we must consider the different nature of films and lyophilized silk fibroin blocks: the first exposes the major part of their surface, while the second exposes only a part of their free surface; in this last case water moisture needs more time to enter inside the pore and plasticize the material. In this step is important to add water without changing the protein conformation into the stable β-parallel form: in fact, an excessive crystallization does not allow the thermal-reflow, as proved from the impossibility to properly sinter a block of lyophilized silk fibroin exposed to a 12 h moisture treatment (**figure 5 (C)**, 12h and LTS 12h). For this reason, we choose to expose the lyophilized silk fibroin to water moisture for a time between 30 and 60 min, enough to add a 20% of water but not sufficient to stabilize the structure into the β-parallel crystalline form. In the third step the fast application of a high pressure allows the fast diffusion of the water in the inner part of the lyophilized block and the thermal-reflow occurs due to the decrement in the glass transition temperature (**figure 1 (A)**, step 5). In the last step the maintenance of a high pressure for about 20 minutes allow to uniform the material and to remove the residual water. We hypothesize the fast decrement of the glass transition temperature due to the high pressure applied, so even if after the addition of the water the T_g of the lyophilized silk fibroin is around 180 °C (**figure 6 (B)**) during the compression its value is decreased under 40 °C allowing the molecular flow to take place. This hypothesis is further confirmed by the microstructural analysis, that reveals the formation of planes at low magnification (**figure 7**, column 1) and ripples at nano and micro scale at high magnification

(**figure 7**, column 2): a "flow" appear to take place before the full compaction. Then the decrease of the water content during the maintenance time and the removal of the pressure shift the T_g to 60 °C (**figure 6 (A)**, Lyo). After the compression (**figure 5 (C)**, LTS 30 m) some alpha structures are formed, and the sample resulted to be higher in β-turns, parallel, and antiparallel β-sheet all at the expense of a decrease in the native β-sheet. Instead the random coil percentage remain unchanged. Cell adhesion to biomaterials is a fundamental step in cell-cell communication and regulation, and tissue regeneration. The biological evaluation on LTS fibroin samples showed interesting results of cell adhesion through different time points and comparable to the results obtained on PCL, material commonly used in biomedical applications[40]. After confocal images evaluation (**figure 8**), we can observe a general and homogeneous cell distribution on both surface samples along time points. However, at day 5 it is possible to observe that, even if PCL surface samples present higher cell density, the cell shape is elongated, indicating that cell-cell interactions are more focused among cells than cell-to-sample surface. On the other hand, on LTS fibroin samples, cells are in a less cell density but their shape is more extended, indicating that the interaction between cells and sample surface is higher, promoting a greater degree of spreading. This behavior can indicate that, since LTS fibroin samples are made of protein, their surfaces offer more adhesion sites to cells, improving the mechanism of interaction between cells and surface.

3. Conclusions

In this work we present a fast method to produce solid fibroin monoliths at low temperature. This method is based on a high-pressure, low-temperature solid-solid transition of lyophilized silk fibroin that occur via thermal-reflow. The process was optimized using a design of experiment method to obtain a full transition from lyophilized silk fibroin to its solid form. In addition, the DOE method revealed useful insight on the process as the important role of the water, and other secondary effects

that are not usually accessible with other methodology. The analysis conducted with FTIR on the main stages of the process revealed that an excessive transition to β-parallel structure, due to a prolongated water treatment, doesn't allow the transition to the solid state; the transition occur if the secondary structures are not enough stable to be able to re-organize them self in more stable phases during the compression phase. The glass transition temperature was individuated by DSC. Interestingly, the rapid addition of water in the material through moisture absorption didn't change the T_g respect the lyophilized silk fibroin. Instead a decrease of almost 120 °C in the T_g has been individuated after the compression. The SEM analysis during different time points in the compression proved the presence of a viscous flow. So, we could deduce a decrease in the T_g under the process temperature (40 °C) when the high pressure is applied to the moisturized lyophilized silk fibroin. The preliminary biological results, showed by confocal imaging, indicate a promising role of LTS fibroin samples in biomedical applications for promoting cell adhesion and proliferation. Overall, we were able to optimize a fast, low temperature method to obtain large monoliths of solid-fibroin, reporting, for the first time a thermal-reflow at 40 °C for lyophilized fibroin. This method could be useful in further study to produce solid fibroin object, in a rapid fashion, for direct compression and to substitute other material commonly used in surgical implants.

4. Experimental Section

Silk fibroin preparation

Extraction and purification of silk fibroin was conducted using an adapted version of a well-known protocol[18]. Briefly, to separate silk fibroin from silk sericin, Bombyx mori silk cocoons has been cut in small pieces and placed in a 0.01 M hot bath of sodium carbonate (Na_2CO_3, Sigma Aldrich) for 1 hour, followed by a second immersion in a bath of sodium carbonate with a concentration of 0.003M for 1 hour. The resultant silk fibroin, progressively taken at room temperature, was carefully rinsed

for 3 times using ultrapure water and then dried for 2 days. The resulting degummed silk fibroin was dissolved into a 9.3 M water solution of lithium bromide (LiBr, Sigma Aldrich) at 60°C for 4 h, then dialyzed against water for 3 days to remove the salt. Finally, the regenerated silk fibroin solution was placed into vials of 15 mL, frozen using liquid nitrogen, and freeze-dried for 3 days to obtain the lyophilized silk fibroin used for the sintering process.

Sintering procedure

The compression of lyophilized silk fibroin was performed on hydraulic universal testing machine equipped with thermostatic chamber allowing the temperature control within a range of ±1 °C (MTS 858 Mini Bionix, Italy) using a stainless-steel mold. The process is represented in **figure 1 (A)**: the regenerated silk fibroin solution (**step 1**) was frozen in liquid nitrogen and then lyophilized (**step 2**) for 3 days at -50 °C; then a single block of lyophilized silk fibroin was placed into a humidostatic chamber with a controlled temperature of 25 °C and a constant humidity of 80 % for a time sufficient to reach a 20% increment in weight, typically between 30 and 60 min. (**step 3**); subsequently, the material was placed inside the mold and a pre-compression of 5 MPa was applied for 60 s (**step 4**) then, the chamber was heated at 40 °C and a compression curve (**step 5**) was applied; finally, the resulting solid-fibroin was extracted from the mold (**step 6**).

An example of compression is shown in **figure 1 (C)**: the maximum pressure (P_{max}) was reached during the ramp time (t_{ramp}), then the pressure was kept constant during the maintaining time (t_{maint}). These three factors and the mass percentage of adsorbed water ($m_{w\%}$) were used to optimize the process in the design of experiment.

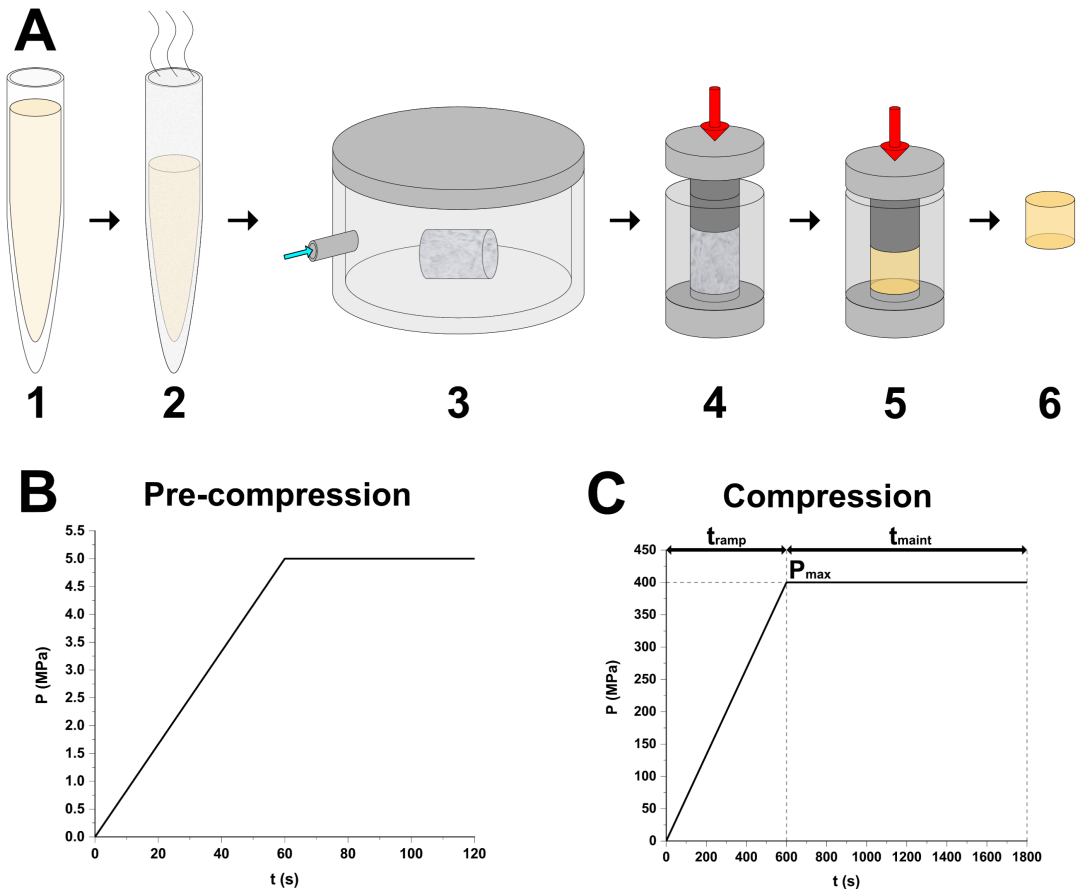

*Figure 8: (A) Steps of the overall process, **1** production of a fibroin solution, **2** rapid cooling with liquid nitrogen and lyophilization, **3** addition of water via moisture absorption in a humidostatic chamber, **4** a pre-compression phase uniform the initial material, **5** the compression phase in which the solid-solid transition occur and the fibroin pass from the lyophilized to the solid state , **6** the extraction from the mold. (**B**) Pressure vs. time pre-compression diagram: the pre-compression phase is the same for all the prepared samples, it consists in a compression ramp of 1 min to reach the pressure of 5 MPa that is maintained for another minute. (**C**) Pressure vs. time compression diagram: a maximum pressure is reached (P_{max}) during the ramp time (t_{ramp}) then this pressure is maintained for the maintaining time (t_{maint}). These three variables and the amount of added water ($m_{W\%}$, as fourth variable) were used to evaluate and optimize the process.*

Design of experiment for the process optimization

Due to the presence of several process parameters, at such a low temperature is extremely difficult to find the best procedure for realizing the complete transition of the lyophilized fibroin to its compact solid state. So, the entire process was optimized with a 2^4 full factorial design of experiment (DOE) considering two levels (+1, -1) for each of the 4 studied parameters. The variables and their respective levels are listed in **table 1**: the ramp time, the maximum pressure and the maintaining time were set directly in the hydraulic press. The last variable refers to use of lyophilized silk fibroin with or without

water adsorption: 20 % is refers to the humidity condition in which the lyophilized silk fibroin was placed into the controlled humidity chamber to allow water adsorption, while 0% refers to the use of dry lyophilized fibroin. The experimental design required the production of 16 samples (**table 1S**) that constitute all the possible combinations of the variables level. To evaluate the transition from lyophilized to solid silk we chose to measure two physical properties: the sample transparency and the mechanical strength. Transparency was evaluated by calculating the area underlying the optical absorbance spectrum in the 400-800 nm range normalized by the sample thickness. These two parameters (yields) are used to build an empirical model that relate their value to the sintering parameters. The general equation for a 2^4 full factorial design is shown in **table 1**. Pareto plot and half-normal plot followed by analysis of variance (ANOVA) test were used to discriminate the terms to be included in the model on the base of their significance ($p<0.005$). The equations are reported with coded dimensionless terms, which implies that the all the variables are considered to vary between -1 and, allowing a direct comparison. For the sake of simplicity, we decide to report in the results section the coded terms in the equations and the real variable values in the graphs.

Variable	+1 level	-1 level
t_{ramp} (s)	600	120
P_{max} (MPa)	400	200
t_{maint} (s)	1200	0
$m_{\%W}$ (% w/w)	20	0

$$Y = c_1 * t_{ramp} + c_2 * P_{max} + c_3 * t_{maint} + c_4 * m_{\%W} + c_5 * t_{ramp} * P_{max} + c_6 * t_{ramp} * t_{maint} + c_7 * t_{ramp} * m_{\%W} + c_8 * P_{max} * t_{maint} + c_9 * P_{max} * m_{\%W} + c_{10} * t_{maint} * m_{\%W} + c_{11} * t_{ramp} * P_{max} * t_{maint} + c_{12} * t_{ramp} * P_{max} * m_{\%W} + c_{13} * t_{ramp} * t_{maint} * m_{\%W} + c_{14} * P_{max} * t_{maint} * m_{\%W} + c_{15} * t_{ramp} * P_{max} * t_{maint} * m_{\%W}$$

Table 1: Considered variables and their respective levels used to build the model equation (bottom). The variables are: the ramp time (t_{ramp}), the maximum applied pressure (P_{max}), the maintaining time (t_{maint}), and the percentage of added water ($m_{\%W}$). The equation includes first order terms, directly correlated to the variables, and higher order "mixed" terms.

Characterization

Using Fourier transform infrared spectroscopy (FTIR) and digital scanning calorimetry (DSC) we observed the variation of secondary structures and the glass transition temperature throughout the process in order to study, at a molecular level, the solid-solid transition process. In particular, we proved that this transition can occur even if the T_g of the initial material is higher than the temperature used in the compression phase. The reduction of the glass transition temperature due to the compression effect on the moisturized material was deduced by SEM microstructural analysis through which the thermal-reflow in the material as a function of the compression time was observed. To determine the parameters influencing the process and their optimum value a design of experiments (DOE) based on two yields has been adopted: the material's transparency and the compressive Young modulus. Compression tests were performed in both dry and wet samples. Finally, to study the potential role of LTS fibroin samples in biomedical applications, we preliminary evaluated their effect

of *in vitro* cell culture. Human adipose-derived mesenchymal stem cells (AdMSCs) were cultured on the samples in static condition and their adhesion and proliferation were studied by confocal analysis.

Optical characterization

UV-Vis spectra, measured on both flat surfaces of each fibroin cylinders (two for each sample), were collected using a Jasco V-570 spectrophotometer (USA), through a black mask with a 6 mm diameter hole. The transparency indexes were evaluated by integrating these spectra on the visible range (from 400 to 700 nm) to obtain the areas, then calculating the average area value for from the two results obtained for each sample and normalizing it for the sample thickness.

Mechanical characterization

Compression tests were made using an Instron 7500 universal testing machine (USA) with a compression rate of 1 mm/min in a controlled environment (25 °C and 20% RH). A pre-compression of 0.2 kN was applied prior the testing. The Young modulus was evaluated as angular coefficient of the curve in the initial elastic (linear) zone.

The same procedure was used to evaluate the compressive young modulus of the material in wet condition at 37 °C, to simulate the environment of a body implant: among 8 silk solid fibroin cylinders produced by the optimized process, 4 were tested immediately after being soaked into water at 37 °C for 6 hours, while the other 4 after keeping it in a desiccator for 48 h at room temperature. The mean and the standard deviation of both groups were then calculated.

Infrared spectroscopy

Assignment	Peak position cm^{-1}
Side chain	1597-1609
Intermolecular parallel β-sheet	1610-1625
Native β-sheet	1626-1635
Random coil	1636-1655
α-helix	1656-1662
B-turns	1663-1696
Intermolecular antiparallel β-sheet	1697-1703

Table 2: Peak positions and their secondary structure assignment used for the primary amide fitting.

The secondary structure changes were evaluated using an ATR-FTIR spectrophotometer (Perkin Elmer, Spectrum ONE, USA). To maximize signal to noise ratio, 32 spectra with a resolution of 1 cm^{-1} were collected and averaged for each sample. The silk fibroin secondary structures were, then, quantitively evaluated analyzing the primary amide peak (1580-1720 cm^{-1}). The peak was smoothed with a 5 points adjacent averaging function followed by a Fourier self-deconvolution (FSD, with smoothing factor of 0.3 and gamma function of 30) to enhance the resolution and better shape the singular components. A second derivative was then performed to identify the peaks position. These values were then used to fit the single peaks with a Gaussian function. The fitting routine was recursively applied until χ^2 was minimized. The ratio between the fitted peak area and the total area was calculated to determine the percentage of the specific structure assigned to the peak[41]. In **table 2** the assigned secondary structure for different bandwidths of the FTIR spectrum is reported[42].

Thermal analysis

A differential scanning calorimetry (DSC, Q20, TA instruments, USA) was used to evaluate the thermal behavior of the samples in the range between 40 and 320 °C. The tests were performed under nitrogen flow (50 mL/min) using hermetic lids and a temperature ramp of 10 °C/min. Modulated DSC was done in the same range using a temperature ramp of 3 °C/min and a modulation amplitude of ± 0.5 °C and a period of 40 s.

Morphological analysis

SEM analysis has been performed in 4 time points of the compression phase (0, 40, 80 and 120 s) to observe the thermal-reflow of the material. The samples were frozen in liquid nitrogen and cut with a blade to reveal the cross-section. The samples underwent to Pt/Pd coat by plasma sputtering prior to SEM observation (FESEM, Zeiss Supra 60, Germany). Distances in the images were estimated by taking 30 measurements and reporting the mean and the standard deviation.

In vitro cell culture and confocal microscopy

Cell adhesion on LTS fibroin cylindrical samples (8 mm diameter, 3 mm height) was evaluated by culturing Adipose-derived Mesenchymal Stem Cells (AdMSCs) gently provided by Technical University of Munich, Germany. AdMSCs where obtained from human adipose tissue healthy donors (N = 3) after written informed patient's consent (study approved by the Local Ethics Committee of the 'Klinikum Rechts der Isar') and isolated from fat tissue using a well-established protocol[43]. Samples with same geometry made of Poly-ϵ-caprolactone (PCL, Sigma Aldrich) were prepared and used as control. All samples were sterilized in autoclave at 121 °C for 15 min, before seeding.

AdMSCs (passage 3), were seeded on samples with a density of $6x10^4$ cells/cm^2 and cells were cultured up to 5 days, at 37 °C and 5% CO_2 in a humidified atmosphere.

After each time point (1, 3, and 5 days), cell adhesion, morphology and distribution were analyzed by confocal microscopy (Nikon A1, Nikon Instruments, Amsterdam, The Netherlands) imaging. Before confocal observations, samples were fixed with 10% formalin solution (40 min, RT) (Sigma Aldrich), permeabilized with 0.2% Triton X-100 in PBS (30 min, RT) (Sigma Aldrich) and stained with CytoPainter Phalloidin-iFlour 488 Reagent (Abcam) to mark actin filament distribution of the cytoskeleton and DAPI (Sigma Aldrich) to mark the nuclei, according to the manufacturer's instructions.

Supporting Information

Supporting Information is available from the Wiley Online Library or from the author.

References

[1] L.-D. D. Koh, Y. Cheng, C.-P. P. Teng, Y.-W. W. Khin, X.-J. J. Loh, S.-Y. Y. Tee, M. Low, E. Ye, H.-D. D. Yu, Y.-W. W. Zhang, M.-Y. Y. Han, *Prog. Polym. Sci.* **2015**, *46*, 86.

[2] C. Jiang, X. Wang, R. Gunawidjaja, Y. H. Lin, M. K. Gupta, D. L. Kaplan, R. R. Naik, V. V. Tsukruk, *Adv. Funct. Mater.* **2007**, *17*, 2229.

[3] B. B. Mandal, A. Grinberg, E. Seok Gil, B. Panilaitis, D. L. Kaplan, *Proc. Natl. Acad. Sci.* **2012**, DOI 10.1073/pnas.1119474109.

[4] B. Kundu, R. Rajkhowa, S. C. Kundu, X. Wang, *Adv. Drug Deliv. Rev.* **2013**, *65*, 457.

[5] G. H. Altman, F. Diaz, C. Jakuba, T. Calabro, R. L. Horan, J. Chen, H. Lu, J. Richmond, D. L. Kaplan, *Biomaterials* **2003**, *24*, 401.

[6] Q. Zhang, S. Yan, M. Li, *Materials (Basel).* **2009**, *2*, 2276.

[7] Y. Cao, B. Wang, *Int. J. Mol. Sci.* **2009**, DOI 10.3390/ijms10041514.

[8] A. Motta, L. Fambri, C. Migliaresi, **2002**, 1658.

[9] L. D. Koh, Y. Cheng, C. P. Teng, Y. W. Khin, X. J. Loh, S. Y. Tee, M. Low, E. Ye, H. D. Yu, Y. W. Zhang, M. Y. Han, *Prog. Polym. Sci.* **2015**, *46*, 86.

[10] P. X. Ma, *Adv. Drug Deliv. Rev.* **2008**, *60*, 184.

[11] N. Kasoju, U. Bora, *Adv. Healthc. Mater.* **2012**, *1*, 393.

[12] F. G. Omenetto, **2014**, 28.

[13] J. J. Amsden, A. Gopinath, L. Dal Negro, D. L. Kaplan, F. G. Omenetto, *2009 Conf. Lasers*

Electro-Optics Quantum Electron. Laser Sci. Conf. (Cleo/Qels 2009), Vols 1-5 **2009**, *007*, 201.

[14] R. K. Pal, A. A. Farghaly, C. Wang, M. M. Collinson, S. C. Kundu, V. K. Yadavalli, *Biosens. Bioelectron.* **2016**, *81*, 294.

[15] B. Zhu, H. Wang, W. R. Leow, Y. Cai, X. J. Loh, M. Y. Han, X. Chen, *Adv. Mater.* **2016**, *28*, 4250.

[16] A. Bucciarelli, R. K. Pal, D. Maniglio, A. Quaranta, V. Mulloni, A. Motta, V. K. Yadavalli, A. Bucciarelli, D. Maniglio, A. Quaranta, A. Motta, V. Mulloni, **2017**, *201700110*, 1.

[17] A. Bucciarelli, V. Mulloni, D. Maniglio, R. K. Pal, V. K. Yadavalli, A. Motta, A. Quaranta, *Opt. Mater. (Amst).* **2018**, *78*, 407.

[18] D. N. Rockwood, R. C. Preda, T. Yücel, X. Wang, M. L. Lovett, D. L. Kaplan, *Nat. Protoc.* **2011**, *6*, 1612.

[19] B. Marelli, N. Patel, T. Duggan, G. Perotto, E. Shirman, C. Li, D. L. Kaplan, F. G. Omenetto, *Proc. Natl. Acad. Sci.* **2017**, *114*, 451.

[20] A. Matsumoto, J. Chen, A. L. Collette, U. Kim, G. H. Altman, P. Cebe, D. L. Kaplan, **2006**, 21630.

[21] J. Magoshi, Y. Magoshi, M. A. Becker, M. Kato, Z. Han, T. Tanaka, S. ichi Inoue, S. Nakamura, *Thermochim. Acta* **2000**, *352*, 165.

[22] K. Liu, Z. Shi, S. Zhang, Z. Zhou, L. Sun, T. Xu, Y. Zhang, G. Zhang, X. Li, L. Chen, Y. Mao, T. H. Tao, *Adv. Healthc. Mater.* **2018**, *7*, 1701359.

[23] T. G. Tirta Nindhia, Y. Koyoshi, A. Kaneko, H. Sawada, M. Ohta, S. Hirai, M. Uo, *Trends Biomater. Artif. Organs* **2008**, *22*, 25.

[24] A. Kaneko, Y. Tamada, S. Hirai, T. Kuzuya, T. Hashimoto, *Macromol. Mater. Eng.* **2012**, *297*, 272.

[25] H. A. Tuan, S. Hirai, Y. Tamada, S. Akioka, *Mater. Sci. Eng. C* **2019**, *97*, 431.

[26] R. M. Daniel, M. Dines, H. H. Petach, *Biochem. J.* **1996**, *317 (Pt 1*, 1.

[27] N. Agarwal, D. a Hoagland, R. J. Farris, *J. Appl. Polym. Sci.* **1997**, *63*, 401.

[28] X. Hu, D. Kaplan, P. Cebe, *Thermochim. Acta* **2007**, *461*, 137.

[29] K. Yazawa, K. Ishida, H. Masunaga, T. Hikima, K. Numata, *Biomacromolecules* **2016**, *17*, 1057.

[30] M. A. Brenckle, B. Partlow, H. Tao, D. L. Kaplan, F. G. Omenetto, *Biomacromolecules* **2013**, *14*, 2189.

[31] M. A. Brenckle, H. Tao, S. Kim, M. Paquette, D. L. Kaplan, F. G. Omenetto, *Adv. Mater.* **2013**, *25*, 2409.

[32] M. A. Brenckle, D. L. Kaplan, F. G. Omenetto, *Adv. Mater. Interfaces* **2016**, DOI 10.1002/admi.201600094.

[33] M. A. Brenckle, B. Partlow, H. Tao, M. B. Applegate, A. Reeves, M. Paquette, B. Marelli, D. L. Kaplan, F. G. Omenetto, *Adv. Funct. Mater.* **2016**, *26*, 44.

[34] Z. Gao, Z. Zhou, H. Tao, N. Qin, in *2018 IEEE Micro Electro Mech. Syst.*, IEEE, **2018**, pp. 498–500.

[35] M. Tsukada, G. Freddi, P. Monti, A. Bertoluzza, N. Kasai, *J. Polym. Sci. Part B Polym. Phys.* **1995**, *33*, 1995.

[36] X. Wang, J. A. Kluge, G. G. Leisk, D. L. Kaplan, *Biomaterials* **2008**, *29*, 1054.

[37] H. Yoshimizu, T. Asakura, **1990**, *40*, 127.

[38] A. Gholami, H. Tavanai, A. R. Moradi, *J. Nanoparticle Res.* **2011**, *13*, 2089.

[39] J. Zhong, X. Liu, D. Wei, J. Yan, P. Wang, G. Sun, D. He, *Int. J. Biol. Macromol.* **2015**, *76*, 195.

[40] B. D. Ulery, L. S. Nair, C. T. Laurencin, *J. Polym. Sci. Part B Polym. Phys.* **2011**, DOI 10.1002/polb.22259.

[41] X. Hu, D. Kaplan, P. Cebe, *Macromolecules* **2006**, *39*, 6161.

[42] U. Shimanovich, F. S. Ruggeri, E. De Genst, J. Adamcik, T. P. Barros, D. Porter, T. Müller, R. Mezzenga, C. M. Dobson, F. Vollrath, C. Holland, T. P. J. Knowles, *Nat. Commun.* **2017**, *8*, 1.

[43] S. Schneider, M. Unger, M. Van Griensven, E. R. Balmayor, *Eur. J. Med. Res.* **2017**, DOI 10.1186/s40001-017-0258-9.